ChemCatChem

Research Article
doi.org/10.1002/cctc.202400991

Chemistry Europe
European Chemical Societies Publishing

www.chemcatchem.org

Solar-Assisted CO_2 Methanation via Photocatalytic Sabatier Reaction by Calcined Titanium-based Organic Framework Supported RuO_x Nanoparticles

Celia M. Rueda-Navarro,[a] Marta González-Fernández,[a] María Cabrero-Antonino,[b] Amarajothi Dhakshinamoorthy,[a] Belén Ferrer,*[a] Herme G. Baldoví,*[a] and Sergio Navalón*[a]

CO_2 reduction by sunlight under mild reaction conditions is a research area of increasing interest expected to favor decarbonization and produce fuels and chemicals in the circular economy. We hereby report on the development of a series of titanium oxide-based solids produced by calcination of MIL-125(Ti)-NH_2 decorated with RuO_x nanoparticles (1 wt%) material at temperatures from 350 to 650 °C and used as photocatalysts for CO_2 methanation under simulated sunlight irradiation (45 mW/cm^2) at $<$200 °C and 1.5 atm total pressure. The material synthesized at 350 °C produced the highest photoactivity of the series (4.73 mmol g^{-1} CH_4 at 22 h and an apparent quantum yield at 400, 500 and 750 nm of 0.76, 0.65 and 0.54%, respectively), comparing favorably with the activities of other MOF-based materials reported so far. Insights into the material's photocatalytic performance and a study of the possible reaction pathways during CO_2 methanation were obtained by electrochemical impedance, electron spin resonance, photoluminescence and *in situ* FT-IR spectroscopies together with transient photocurrent and hydrogen temperature programed desorption measurements. The study showed the possibility of using MOF-based materials as precursors to develop metal oxide photocatalysts with enhanced activities for solar-driven gaseous CO_2 photomethanation.

1. Introduction

Burning anthropogenic fossil fuels is currently the predominant method of satisfying the world's energy demand.[1] a process that emits millions of metric tons of CO_2 to the atmosphere every year, one of the greenhouse gases responsible for global warming and climate change. In this context, there is a general scientific commitment to mitigate these undesirable effects for the sake of both the environment and mankind. These actions include several international agreements focused on developing sustainable alternative energy vectors to fossil fuels, such as green hydrogen generated by solar light. These actions are complemented by other strategies, including carbon capture storage and utilization (CCSU) to favor decarbonizing the world's economies.[1–5] Regardless of the important achievements made so far in the CCSU area, transforming CO_2 into added-value chemicals or fuels is still a developing field. One of the challenges involved in this technology is the use of energy inputs based on renewable resources, in which thermocatalytic reduction of CO_2 by green hydrogen is particularly envisioned as a medium-long term economic process.[6] For more than forty years, many efforts have focused on developing an efficient photocatalytic version of the Sabatier reaction under relatively mild reaction conditions.[7] Regardless of the favorable thermodynamics of this reaction ($CO_2 + 4\ H_2 \rightarrow CH_4 + 2\ H_2O_{(g)}$ $\Delta G°$ 298 K = −27 kcal mol^{-1}), the eight-electron reduction process is accompanied by high kinetic energy barriers frequently overcome by high reaction temperatures (300–400 °C) and sometimes by high pressures (*ca* 20 bar). Besides, several studies have reported the importance of the development of new heterogeneous photocatalysts in terms of CO_2 conversion and CH_4 selectivity through the Sabatier reaction.[8–12] The proposed order of activity decreases based on the nature of the metal as follows Ru > Rh > Ni > Fe > Co > Os > Pt > Ir > Mo > Pd > Ag > Au, while the selectivity decreases in the order of Pd > Pt > Ir > Ni > Rh > Co > Fe > Ru > Mo > Ag > Au.[9,11] Regardless of these orders of activity, the reported activity and selectivity also depends on the nature of solid catalyst and the reaction conditions (i.e. temperature, pressure) employed. For example, in thermodynamic equilibrium the Sabatier reaction in terms of CO_2 conversion to CH_4 is favored at high pressures. Regarding the reaction temperature, CO_2 conversion and CH_4 selectivity increases along the temperature. However, further increase of the reaction temperature can cause a decrease in CH_4 selectivity and is attributed in some cases to the occurrence of the reverse waster gas shift reaction ($CO_2 + H_2 \leftrightarrow CO + H_2O$ $\Delta H° = 41$ kJ/mol). For practical applications, the thermocatalytic Sabatier reaction

[a] C. M. Rueda-Navarro, M. González-Fernández, A. Dhakshinamoorthy, B. Ferrer, H. G. Baldoví, S. Navalón
Departamento de Química, Universitat Politècnica de València, Camino de Vera s/n, Valencia 46022, Spain
E-mail: bferrer@qim.upv.es
hergarba@cam.upv.es
sernaol@doctor.upv.es

[b] M. Cabrero-Antonino
Instituto de Tecnología Química (UPV-CSIC), Universitat Politècnica de València, C/Avenida de los Naranjos s/n, Valencia 46022, Spain

Supporting information for this article is available on the WWW under https://doi.org/10.1002/cctc.202400991

is somehow limited due to the relative slow kinetics of the process that requires considerable energy inputs in terms of pressure and temperature while requiring affordable, stable, active and selective heterogeneous catalysts for this purpose. Besides, commercialization of the process depends on CO_2 generation from wastes (i.e. biomass, power plant, industry) while H_2 obtained from renewable energy.[12]

There is therefore an essential need to develop an economically viable catalytic process that operates under milder reaction conditions.[13] In this context, it should be pointed out that several studies have already shown that the light-assisted photocatalytic Sabatier reaction using metal oxides, carbon-based materials and, more recently, metal-organic frameworks (MOFs) can be carried out at relatively lower reaction temperatures ($<200\,^{\circ}C$) and pressures (<2 bar) than the thermocatalytic process while achieving greater efficiency.[6] The successful development of these technologies would provide large-scale CO_2 recycling into CH_4 as a renewable substitute of natural gas and could be implemented in the existing industrial infrastructure.

The photocatalytic Sabatier reaction from MOFs was first reported in a study in 2019,[14] in which a Zn-based MOF was found to be a photocatalyst capable of reducing CO_2 to CH_4 under UV-Vis light irradiation at 215 °C. The presence of Cu_2O in this MOF increased the activity up to 45 $\mu mol\,g^{-1}$ in 24 h and served as a proof-of-concept for the potential use of MOF-based materials as photocatalysts. Since then, other studies have reported Ti-based MOFs as active photocatalysts like MIL-125(Ti)-NH_2,[15] MIP-207(Ti)[16] or Zr-MOFs like UiO-66(Zr/Ti)-NO_2[17] or UiO-66(Zr/Ce/Ti)[18] supported RuO_x nanoparticles (NPs) as co-catalysts. Of these, RuO_x NPs (10 wt%) supported MIL-125(Ti)-NH_2 was reported in 2022 as a benchmark photocatalyst for the solar-assisted Sabatier reaction at 200 °C under batch reaction conditions, achieving a CH_4 production of 18.5 $mmol\,g^{-1}$ after 22 h.[15]

A series of related studies have also reported that MOFs, whether or not modified with metal salts, can be thermally decomposed under inert or oxidative atmospheres to their corresponding metal oxides with enhanced photocatalytic activities.[19–25] Most of these MOF-derived solids (DMOFs) have been used as advanced oxidation photocatalysts in water treatment,[19–24] and to a lesser extent to generate solar fuels.[22,25] The enhanced photocatalytic activities found in these DMOFs are partially attributed to the intrinsic physico-chemical and textural properties of the MOF precursors that result in the formation of C- or N-doped materials with enhanced photo-induced charge separation,[20] sometimes accompanied by graphitic carbon, which favors the photothermal reaction pathway even under infrared irradiation.[19,23,26] The reader is referred to several reviews on this topic for a detailed explanation.[19,20]

In the field of the photocatalytic Sabatier reaction using DMOFs as photocatalysts, for the first time in 2021, Gascon, Garzon-Tovar et al. produced a nickel oxide-based solid derived from optimized pyrolysis of MOF-74(Ni) at 600 °C as the active photocatalyst for CO_2 methanation under concentrated UV-Vis-IR irradiation from a Xe lamp (4,300 mW/cm,^{2} total pressure 5 bar, temperatures of about 275 °C) that achieved high photo-methanation activity (488 $mmol\,g^{-1}\,h^{-1}$ of CH_4).[26] Since then, other publications have reported highly active materials based on Ni/ZrO_2[27] or Ru@ZrO_2[28] obtained from pyrolysis of UiO-66(Zr) solids modified with the corresponding metal salt precursors and used as photocatalysts for CO_2 methanation at temperatures and concentrated UV-Vis-IR light of about 400 °C/2,900 mW/cm^2 and 300 °C/2,400 mW/cm^2, respectively. However, to the best of the authors' knowledge, the possibility of synthetizing Ti-based DMOFs as heterogeneous photocatalysts for the Sabatier reaction have not yet been reported.[29,30]

With these precedents in mind, this work reports on the development of photocatalytically active DMOFs from benchmark RuO_x(1 wt %)@MIL-125(Ti)-NH_2 (RuO_x-DMOF), the precursor of the solar-assisted Sabatier reaction under relatively mild reaction conditions ($<200\,^{\circ}C$ and total pressure of 1.5 bar). The influence of the calcination temperature of the MOF precursor on the photocatalytic activity of DMOFs was studied. The materials were characterized by a series of techniques including powder X-ray diffraction (PXRD), thermogravimetric analyses (TGA), isothermal N_2 sorption measurements, combustion elemental analyses, UV-Vis diffuse reflectance spectroscopy (UV-Vis DRS), X-ray photoelectron spectroscopy (XPS), scanning (SEM) and transmission (TEM) electron microscopies coupled with an energy dispersive X-ray (EDX) detector, among others. These solids were then tested as heterogeneous photocatalysts for CO_2 hydrogenation. The materials were further characterized by electrochemical impedance (EIS), photoluminescence (PL), *in situ* FT-IR, and electron spin resonance (ESR) spectroscopies together with TPD-H_2 and transient photocurrent measurements to determine the photocatalytic activities involved and the possible reaction pathways.

Experimental Section

Materials

Chemicals and reagents used in this work were of analytical or high-performance liquid chromatography (HPLC) grade and supplied by Merck.

Photocatalyst Preparation, Characterization Techniques and Photocatalytic Activity

MIL-125(Ti)-NH_2 solid was prepared by a solvothermal method as previously reported.[15,31] Then, RuO_x NPs (1 wt % of Ru) were supported in this MOF by the photodeposition method.[15] The resulting material was labeled as RuO_x@MIL-125(Ti)-NH_2.

DMOFs materials were obtained by calcination of RuO_x@MIL-125(Ti)-NH_2 in a muffle furnace at 350, 450, 550, or 650 ° C for 4 h and the resulting samples are termed as RuO_x-DMOF-350, RuO_x-DMOF-450, RuO_x-DMOF-550, RuO_x-DMOF-650, respectively.

Details about synthetic procedures (Section S1), characterization techniques (Section S2) and photocatalytic activities (Section S3) employed in this work can be found in supplementary information (SI).

2. Results and Discussion

2.1. Photocatalyst Characterization

The characterization of MIL-125(Ti)-NH_2 agrees with the published data[15] on the formation of a crystalline (PXRD; Figure S1a), porous (1,333 m^2/g; Figure S1b) MIL-125(Ti)-NH_2 solid with a nanoplate-like morphology (377 ± 138 nm) (Figures S1c and d), thermal stability up to about 300 °C (TGA, Figure S1e), UV-Vis DRS (Figure S1f). The presence of supported RuO_x NPs (1.56 ± 0.6 nm) as reveled by TEM (Figure S2d) UV-Vis DRS; Figure S2c) at 1 wt% Ru loading based on inductively coupled plasma - optical emission spectrometry (ICP-OES) analyses.

The influence of the calcination temperature of RuO_x@MIL-125(Ti)-NH_2 on the resulting physico-chemical, textural and electronic properties of RuO_x-DMOFs was then studied. PXRD characterization (Figure 1) of the calcinated materials at temperatures from 350 to 650 °C resulted in the formation of RuO_x-DMOF solids with a crystalline anatase phase accompanied by increasing proportions of rutile phase as the calcination temperature increased.[32] These results agree with the related studies showing that calcination of MIL-125(Ti)[33] or MIL-125(Ti)-NH_2[34] results in a mixed-phase consisting of anatase and rutile, the highest is the calcination temperature, an increased proportion of rutile phase has been reported. Related studies about TiO_2 synthesis by various methods have found that the initial crystalline TiO_2 phase formed is anatase.[35] This anatase phase can be transformed at different extents into rutile phase in the range of about 400–1200 °C. This transformation is not instantaneous and depends on the sample and thermal treatment conditions, among other possible factors temperature and time determine the mixed-phase proportion in the resulting solid. From a structural and thermodynamic point of view, it has been proposed that anatase formation is a less-constrained molecular construction compared to rutile, a process that has also favored due to the lower surface free energy of the anatase phase. The reader is referred to some existing reviews about anatase to rutile phase transformation for a deeper understanding of this process.[35] The absence of diffraction peaks associated with the presence of RuO_x NPs was due to the low Ru loading in the samples (1 wt% as revealed by ICP-OES analyses) and/or small RuO_x NPs (1.74 ± 0.08 nm average particle size and standard deviation of RuO_x-DMOF samples, respectively) as evidenced by TEM measurements and commented below (see Figure 2).

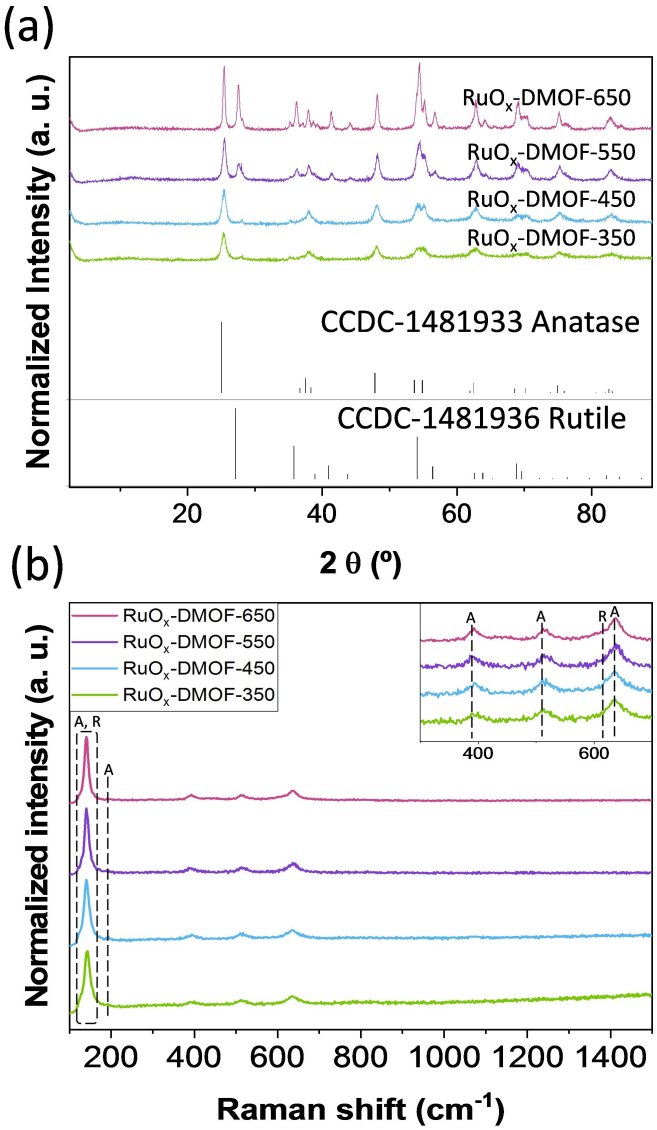

Figure 1. (a) PXRD of RuO_x-DMOF solids and simulated patterns of TiO_2 anatase and rutile phases. (b) Raman spectra of RuO_x-DMOF materials. Inset legend: A and R refer to anatase and rutile, respectively.

Characterization of RuO_x-DMOF solids by Raman spectroscopy (Figure 1b) showed bands attributable to anatase and rutile TiO_2 phases, in agreement with the PXRD analyses.[36] The absence of Raman bands in these spectra at around 1590 and 1371 cm^{-1} discounted the presence of detectable amounts of carbon species with graphitic and defective structures, respectively, while the absence of a band at 1500 cm^{-1} indicated the absence of amorphous carbon in the solids.[37,38] However, combustion elemental analysis of RuO_x-DMOF-350 confirmed the presence of carbon (0.22 wt%) and nitrogen (0.05 wt%) atoms in decreasing proportions for analogous samples prepared at higher calcination temperatures, like RuO_x-DMOF-650 (C 0.1 and N 0.02 wt%) (Table S1). The presence of carbon and nitrogen elements in the samples is consistent with previous studies that found that calcination of MIL-125(Ti)-NH_2 materials formed C-[23] and/or N-doped[24] TiO_2 structures. In general, TGA analyses showed that the samples are thermally stable up to about 500 °C (Figure S3).

The DMOF samples morphology and composition were studied by SEM (Figure S4) and TEM (Figures S5–S8) measurements. In general, these solids had plate-like morphologies with smaller sizes (246 ± 103 nm, Table S2) than their RuO_x@MIL-125(Ti)-NH_2 precursor (377 ± 138 nm) (Figure S4, Table S2), in line with the MOF structure collapse during calcination and transformation into a titanium oxide-based material. In fact, the isothermal N_2 sorption analyses revealed that RuO_x-DMOFs show a gradual decrease in surface area from 127 to 24 m^2/g and pore volume from 0.51 to 0.007 cm^3/g when calcination temperature is raised from 350 to 650 °C, respectively (Table S2, Figure S9). The SEM-EDX analyses for RuO_x-DMOFs revealed that

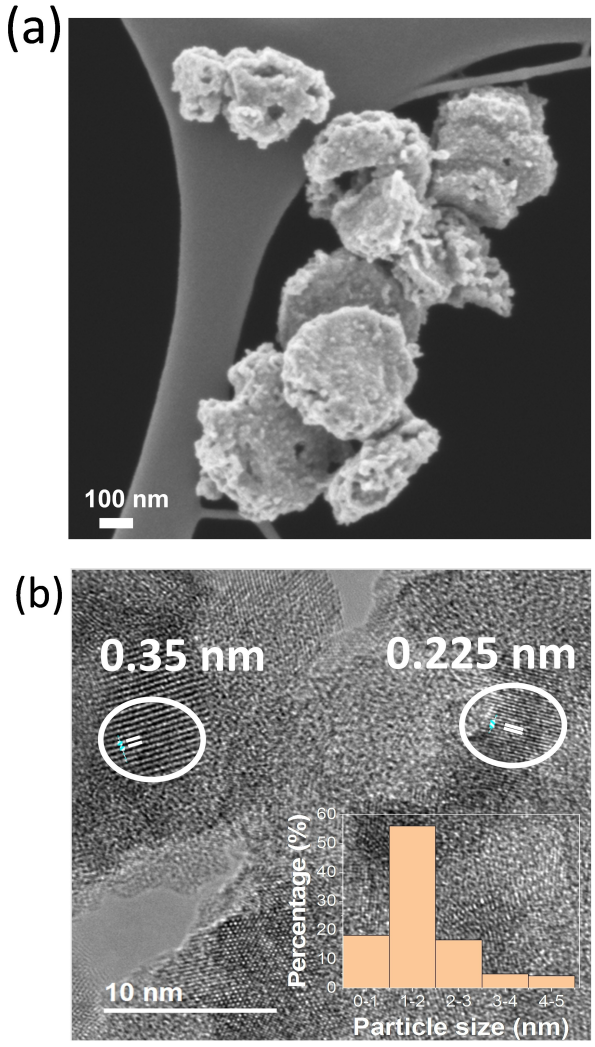

Figure 2. (a) SEM and (b) TEM images of RuO_x-DMOF-350. Panel (b) includes also the RuO_x particle size distribution.

the elements were well distributed throughout the particles (Figures S10–S12).

HRTEM measurements (Figures S5–S8) were also performed to characterize the RuO_x-DMOF solids. In general, all RuO_x-DMOF samples exhibit an RuO_x average particle size of about 1.74 nm. In addition, the lattice spacings of 0.35 nm measured in TEM images were associated with (101) planes of anatase TiO_2 (Figures S7 and S8),[39] while the presence of dark spots with a crystalline support was assigned to RuO_x NPs supported on TiO_2 (Figures S5–S8). The lattice fringes measured on these dark spots with a d-spacing of about 0.225 nm was consistent with the (200) planes of supported RuO_2 (Figures S5–S8).[18]

XPS was used to characterize the elements present in RuO_x-DMOF solids (Figures S13–S17).[32] The analyses revealed the presence of titanium and oxygen elements accompanied by carbon, nitrogen and ruthenium. Ti 2p XPS showed the presence of two bands at 458.1 and 463.7 eV associated with 2 $p_{3/2}$ and 2 $p_{1/2}$ of Ti(IV), respectively, in TiO_2. It should be noted that pristine TiO_2 is characterized by a Ti 2 $p_{3/2}$ at about 459 eV, so that the lower Ti 2 $p_{3/2}$ binding energy observed in RuO_x-DMOF-350 (458.1 eV) can be attributed to the partial replacement of oxygen atoms by the less electronegative nitrogen and/or carbon elements.[24] The absence or negligible Ti 2p signals at about −455, −456 or −457 eV, respectively, indicated that neither Ti–C, Ti(III) nor Ti–N species are formed or present in sufficient proportions to be detected by XPS.[40,41] The XPS O 1s region showed a band at 529.4 eV attributable to lattice oxygen from bulk O^{2-} in TiO_2 or RuO_x while the band at 531.9 eV was attributable to metal hydroxides (Ti–OH or Ru–OH) and/or C–O or Ti–O–C species, respectively.[32,33] The C 1s + Ru 3d XPS region had a broad and relatively intense band at 284.8 eV that could be due to adventitious carbon from the XPS device[40,42,43] and possible overlapping with C-doped TiO_2 in RuO_x-DMOFs. The two other bands at 285.6 and 288.3 eV could also be associated with the presence of C–N or C–O/carbonate species, respectively, within the TiO_2 framework.[23] It should be remembered that the amount of carbon present in RuO_x-DMOFs is below 0.22 wt% as revealed by combustion elemental analyses (Table S1), so that most of the observed C 1s band should be related to the presence of adventitious carbon. The broad band centered at 280.9 eV was associated with the presence of Ru species in different oxidation states.[18] Binding energies below 280 eV can be assigned to the Ru 3 $d_{5/2}$ of metallic Ru(0), while the signals around 281.4 eV were assigned to Ru 3 $d_{5/2}$ of RuO_2 or RuO_x species.[15] The XPS N 1s region is characterized by a band centered at 399 eV associated with the presence of pyrrole-like nitrogen with nitrogen atoms forming M–O–N and/or M–N–O (M: Ti or Ru) linkages, as previously reported.[42] The absence of signals at about 396 eV indicated the absence of Ti–N or Ti–C linkages, in agreement with the XPS Ti 2p spectra.[41]

The optical properties of RuO_x-DMOFs materials were studied by UV-Vis DRS (Figure 3a). These spectra are characterized by absorption bands below 380 nm, mainly consistent with electronic transitions of Ti–O bonds in anatase TiO_2. A small shoulder was observed at about 415 nm associated with Ti–O electronic transitions of the rutile TiO_2 phase. Previous studies showed that TiO_2 valence and conduction bands are mainly assigned to O 2p and Ti 3 d states, respectively.[44] The visible absorption region up to about 425 and 550 nm can be respectively assigned to TiO_2 doping by carbon[23] and nitrogen[24] elements by replacing oxygen atoms in the metal oxide. As reported, C– and N– TiO_2 doping generates C 2p and N 2p valence band states close to those of the conduction band O 2p, a situation that favors visible light absorption, unlike undoped TiO_2. As previously commented, a small proportion of carbon (< 0.22 wt%) and nitrogen (< 0.05 wt%)[24] elements were previously characterized within RuO_x-DMOFs by combustion elemental analyses (Table S1). The presence of Ru-based species in RuO_x-DMOFs can also contribute to UV and Vis absorptions due to Ru–O electronic transitions and surface resonance plasmonic effects, respectively.[45]

The energy band level diagrams of RuO_x-DMOF solids were estimated to determine their thermodynamic properties to be used as photocatalysts for CO_2 reduction by H_2 (Figure 3b). The optical band gaps and maximum valence band positions of these solids were respectively determined from the Tauc plot

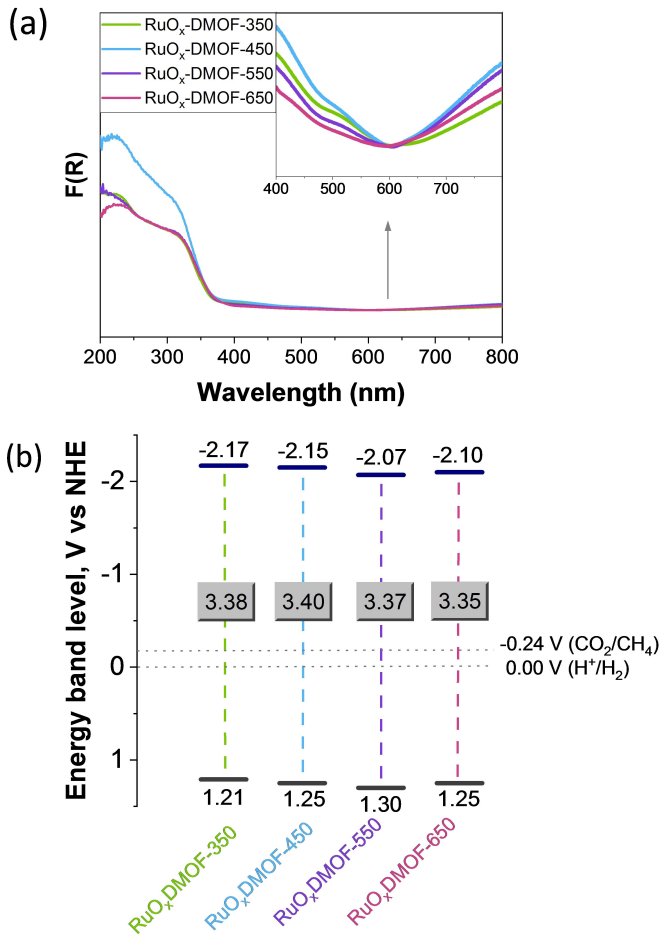

Figure 3. (a) UV-Vis DRS of RuO_x-DMOFs. (b) Energy band level diagram of RuO_x-DMOFs solids.

graph using UV-Vis DRS absorbance data (Figure S18) and valence band XPS measurements (Figure S19) (the details can be found in SI). In general, RuO_x-DMOFs are characterized by optical band gap values of about 3.35 eV with valence band maximum and conduction band minimum values of about +1.3 and −2.1 V, respectively. These results indicate that RuO_x-DMOFs can be used as photocatalysts for CO_2 methanation by H_2.

2.2. Photocatalytic Activities

RuO_x-DMOF samples were tested as photocatalysts for solar-assisted gaseous CO_2 reduction by H_2. The relatively mild reaction conditions consisted of simulated sunlight irradiation with an irradiance value of 45 mW/cm^2, 200 °C and total pressure of 1.5 bar (H_2:CO_2 4:1 molar ratio). Solar irradiance varies from 0 mW/cm^2 at night to about 100 mW/cm^2 (1 sun) on a sunny day, while the actual values are highly dependent on location and local weather, so that we used irradiance conditions to represent an intermediate value between maximum and minimum solar data. Figure 4a shows that the performance of RuO_x-DMOF-350 solid is the most active photocatalyst (4.73 mmol g^{-1} CH_4 production in 22 h), followed by RuO_x-DMOF-450~RuO_x-DMOF-550 (3.62 and 3.33 mmol g^{-1} CH_4 production in 22 h, respectively) and RuO_x-DMOF-650 (2.66 mmol g^{-1} CH_4 production in 22 h). RuO_x-DMOF-350 exhibited a CO_2 conversion of ~11.1 % and selectivity to CH_4 of 99.7 % accompanied by ethane. It is remarkable to note that the optical band gap values of the as-synthetized RuO_x-DMOFs at different calcination temperatures do not vary significantly but, however, they exhibit different photocatalytic activities. In contrast, there is a positive correlation between the photocatalytic activity and the porosity of RuO_x-DMOF solids (*ca.* from 127 to 41 m^2/g) associated to the more favorable diffusion of reactants and products during the reaction along with pores. Furthermore, as will be shown below (Section 2.3. Photocatalytic reaction pathways), this order of photocatalytic activity also correlated with photoinduced charge separation efficiency of the photocatalysts based on transient photocurrent and PL measurements as well as with their charge transfer resistance values determined by EIS characterization. Specifically, RuO_x-DMOF-350 exhibited the highest photoinduced charge separation efficiency and the lowest charge transfer resistance. In addition, it will be shown that the highest photocatalytic activity of RuO_x-DMOF-350 sample compared to RuO_x-DMOF-650 is ascribed to the higher RuO_x reducibility of the former based on the evidence from TPD-H_2 facilitating the formation of metallic Ru(0) species which are responsible for the H_2 activation.[46] In summary, the observed order of photocatalytic activity of RuO_x-DMOFs is correlated with several properties including porosity, photoinduced charge separation efficiency, charge transfer resistance and easier RuO_x reducibility. Attempts to prepare a new sample by calcination of RuO_x@MIL-125(Ti)-NH_2 at lower calcination temperatures (*ca.* 300 °C) resulted in a sample labelled as RuO_x-DMOF-300 that exhibiting slightly lower photocatalytic activity (4.52 mmol g^{-1} CH_4 production in 22 h) than RuOx-DMOF-350. Thus, characterization of RuO_x-DMOF-300 by PXRD (Figure S20a) and Raman spectroscopy (Figure S20b) revealed that this solid shows characteristic features of TiO_2 anatase phase accompanied with low intense diffraction peaks of rutile. SEM analyses revealed that RuO_x-DMOF-300 is constituted by solid particles of about 278 ± 91 nm (Figure S21) while TEM measurements revealed the presence of RuO_x NPs (1.59 ± 0.26 nm) within the TiO_2 matrix (Figure S22). RuO_x-DMOF-300 is also characterized by UV-Vis DRS and Tauc plot analysis, thus allowing to estimate an optical band gap of 3.33 eV (Figure S23).

Continuing with the most photoactive sample prepared in this study, a control experiment showed that the activity of RuO_x-DMOF-350 in the dark at 200 °C is about four-times lower (1.1 mmol g^{-1} after 22 h) than under simulated sunlight irradiation (Figure 4c). The observation of thermocatalytic activity using RuO_x-DMOF-350 under dark conditions agrees with the well-known role of the RuO_x species as co-catalysts for CO_2 methanation.[47] In another control experiment, the use of bare DMOF-350 solid as a photocatalyst resulted in the production of only 9.8 μmol g^{-1} CH_4 after 22 h, highlighting the importance of RuO_x NPs as co-catalysts to achieve high activity. Further, an analogous experiment under dark reaction conditions resulted

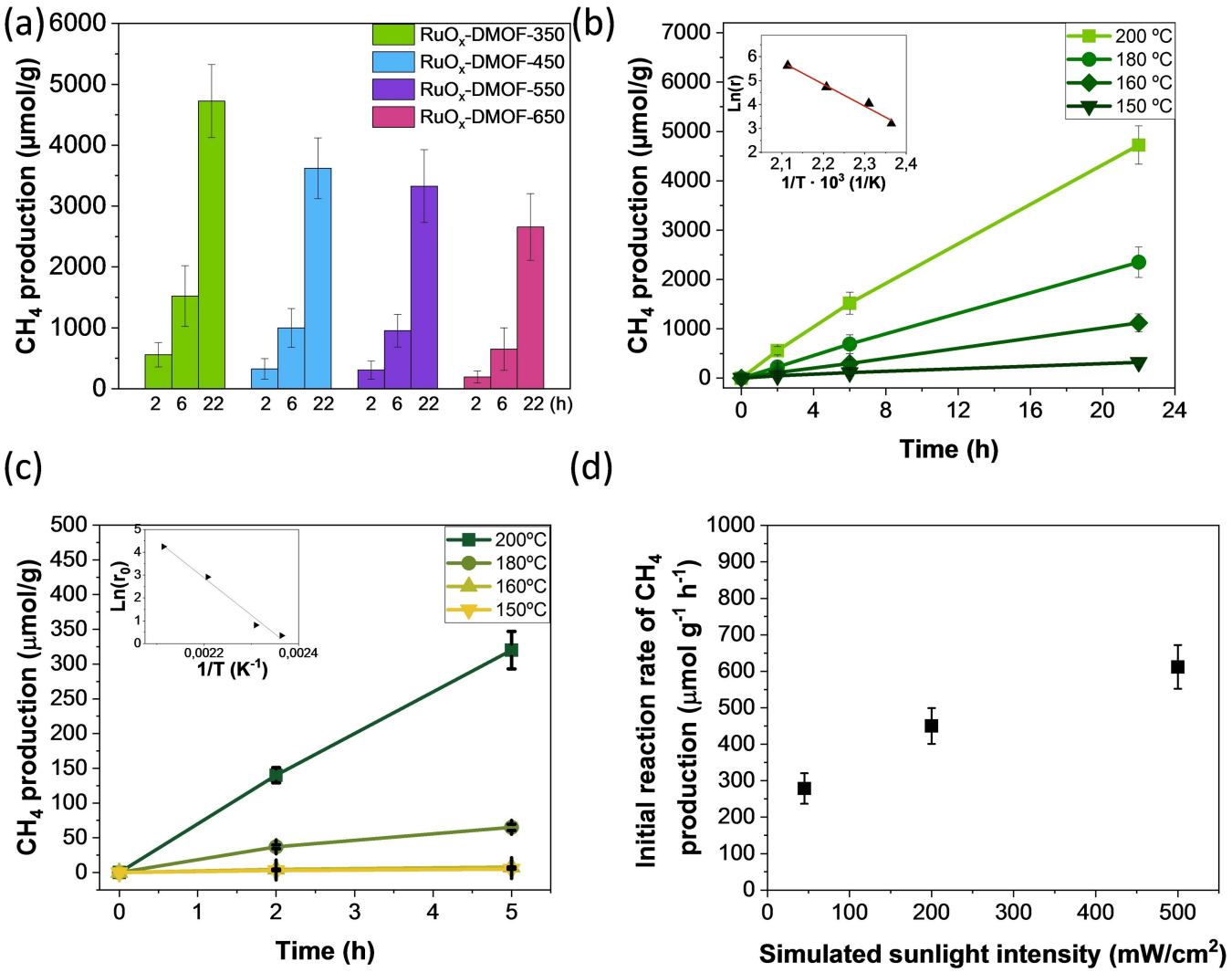

Figure 4. (a) Photocatalytic activities during CO_2 methanation using RuO_x-DMOFs at 200 °C. (b) Influence of reaction temperature on CH_4 generation during photocatalytic CO_2 reduction using RuO_x-DMOF-350. The inset shows the Arrhenius plot obtained from initial reaction rates of CH_4 generation as a function of the reaction temperature. Reaction conditions: Photocatalyst (15 mg), P_{CO2} (0.3 bar), P_{H2} (1.2 bar) under simulated sunlight irradiation (45 mW/cm^2) and (c) photocatalytic CO_2 reduction in the dark. (d) Influence of simulated sunlight intensity on CH_4 generation during photocatalytic CO_2 reduction with RuO_x-DMOF-350 solid at 200 °C.

in even lower CH_4 generation (5.8 µmol g^{-1} of CH_4 after 22 h) associated to the positive role of the sunlight irradiation determining the activity of this catalyst. A photocatalytic experiment using labeled $^{13}CO_2$ and H_2 using RuO_x-DMOF-350 showed the formation of $^{13}CH_4$ in GC-MS analysis (Figure S24). CH_4 and other products were not formed in another photocatalytic control experiment using RuO_x-DMOF-350 in which CO_2 was replaced by Ar. In short, these experiments confirmed the ability of RuO_x-DMOF-350 as the (photo)catalyst in CO_2 hydrogenation to CH_4.

The influence of reaction temperature and light irradiation intensity on the resulting (photo)catalytic activities for CO_2 reduction by RuO_x-DMOF-350 was then studied. The data obtained from photocatalytic and thermocatalytic experiments followed the Arrhenius model and allowed the apparent activation energies of these processes to be estimated with the values of 77 and 151 kJ/mol, respectively. A quasi-linear correlation was found between photogenerated CH_4 and light intensity (Figure 4d). These two latter observations, i.e. the decrease of E_a under irradiation together with the observation of quasi-linear photocatalytic CH_4 generation as a function of irradiation intensity, can be associated with the operation of a dual thermo- and photochemical reaction mechanism[30] as will be further investigated in Section 2.3.

The RuO_x-DMOF-350 photocatalyst was used four consecutive times without a significant reduction in activity (Figure 5a), while the PXRD of the four-times used solid for 88 h retained its initial crystallinity (Figure 5b). Raman (Figure S25), SEM-EDX (Figure S26). HR-TEM analyses showed that the four-times used photocatalyst had a similar RuO_x average particle size distribution and standard deviation (1.84 ± 0.77 nm) (Figures S27a and S28) as the fresh sample (1.73 ± 0.92 nm) (Figures 2 and S5). The UV-Vis DRS of fresh and used photocatalysts showed practically the same absorption features (Figure S27b).

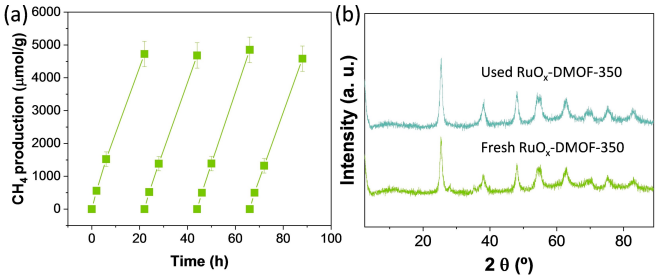

Figure 5. (a) Reusability of RuO_x-DMOF-350 for CO_2 photomethanation. (b) PXRD of fresh and four-times used RuO_x-DMOF-350. Same reaction conditions as described in Figure 4a.

XPS comparison of the fresh and four-times used photocatalysts (Figures S27c and S27d) did not reveal significant modifications in the XPS regions for C 1s, N 1s, Ru 5d or Ru 3p. In contrast, the XPS O 1s band of the used photocatalyst shifted slightly to the higher binding energies and could have been associated with the presence of adsorbed CO_2 species or other possible reaction compounds.

The photocatalytic activity of RuO_x-DMOF-350 during gaseous CO_2 hydrogenation was then compared with that achieved using related MOF-derived and MOF-based materials (results summarized in Table 1). Care should be taken when comparing the photocatalysts' performance published in the literature, especially in terms of micro- or millimole per gram of photocatalyst, due to the different reactor configurations, light intensity, artificial (i.e. UV-Vis, Vis, simulated sunlight) or natural sunlight irradiation, co-catalyst loading and reaction temperature, among other possible factors (Table 1, entries 1–4). For example, MOF-74(Ni)-derived photocatalyst reached an activity as high as 488 mmol g^{-1} h^{-1} under high intensity UV-Vis-IR irradiation (4,300 mW/cm^2), 5 bars of total pressure and temperatures of about 275 °C, while the activity under natural sunlight irradiation at 27.8 °C was about 1.1 mmol g^{-1} h^{-1}. The reaction conditions we used in this study and other similar ones (Table 1, entries 2–4) differ significantly from the relatively milder reaction conditions used for RuO_x-DMOF-350. Interestingly, RuO_x-DMOF-350 showed a comparable photocatalytic performance to some of the most active MOF-based photocatalysts, such as UiO-66(Zr/Ti)-NO_2 or MIL-125(Ti)-NH_2 supported RuO_x NPs (1 wt% Ru loading) in spite of the lower irradiance conditions in the former case (Table 1, entry 2 vs entries 4 and 5). The activity of RuO_x-DMOF-350 (1 wt% Ru) using much lower solar light irradiance was found to be almost double that achieved using RuO_x@MIL-125(Ti)-NH_2 (2 wt % Ru) (Table 1, entry 7). These observations highlight the advantageous properties of DMOF-based photocatalysts compared to MOFs.

In the quest for a more reliable comparison of photocatalytic activities between different materials, several studies have proposed using the apparent quantum yield (AQY) parameter at specific wavelengths. In the present study, AQY values were estimated for the RuO_x-DMOF-350 sample and subtracting the photocatalytic activity achieved under monochromatic irradiation in the dark. The estimated AQY values under irradiation at 400, 500 and 750 nm were found to be 0.76, 0.65 and 0.54%, respectively. This parameter, however, was not considered to quantify the DMOF activity given in Table 1 (Entries 1–4). The AQY values of RuO_x-DMOF-350 are remarkably higher than those achieved from RuO_x(1 wt% of Ru)@UiO-66(Zr/Ti)-NO_2 (0.25 and 0.01% at 400 and 600 nm, respectively), one of the most active MOF-based photocatalyst reported recently.[17]

2.3. Photocatalytic Reaction Pathways

As demonstrated in Section 2.2., RuO_x-DMOF-350 exhibited the highest photocatalytic activity for the selective gaseous CO_2 hydrogenation to CH_4. Additional spectroscopic analyses were performed to further support these findings. It should be noted that similar previous studies using supported RuO_x NPs on traditional inorganic semiconductors like TiO_2[7] or MOF-based photocatalysts[15,18] like MIL-125(Ti)-NH_2- or UiO-66-based also found high selectivity of CO_2 methanation by H_2. This high

Table 1. Photocatalytic activities achieved during gaseous and selective CO_2 methanation using DMOF or MOF-based photocatalysts reported in the literature.

Entry	Catalyst	Reaction conditions	CH_4 production	Ref.
1	DMOF from MOF-74(Ni)	Photocatalyst (30 mg), total pressure 5 bar (H_2/CO_2 = 4), temperature (about 275 °C) irradiation with UV-Vis-IR (4,300 mW/cm^2)	488 mmol g^{-1} h^{-1}	[26]
2	Ni@C-600 from MOF-74(Ni)	Photocatalyst (30 mg), total pressure 5 bar (H_2/CO_2 = 4), temperature (27.8 °C), natural sunlight irradiation	1.1 μmol g^{-1} h^{-1}	[26]
3	Ni/ZrO_2 from UiO-66(Zr)-Ru–Ni(II)	Photocatalyst (10 mg), reaction mixture [10% CO_2/40% H_2/50% He], flow (25 mL/min), temperature (394 °C), irradiation with UV-Vis-IR (2,900 mW/cm^2)	583.3 mmol g^{-1} h^{-1}	[27]
4	Ru@ZrO_2 from UiO-66(Zr)-Ru(III)	Photocatalyst (30 mg), reaction mixture (H_2:CO_2 4:1 molar ratio), space velocity (10,000 N mL g^{-1} h^{-1}), reaction temperature (300 °C), irradiation with visible led (2,400 mW/cm^2)	65 mmol g^{-1} h^{-1}	[28]
5	RuO_x@UiO-66(Zr/Ti)-NO_2	Photocatalyst (15 mg), CO_2:H_2 (1:4), total pressure 1.5 bar, 200 °C, simulated concentrated sunlight (200 mW/cm^2) irradiation.	5.03 mmol g^{-1} after 22 h	[17]
6	RuO_x(1 wt%)@MIL-125(Ti)-NH_2	Photocatalyst (15 mg), CO_2:H_2 (1:4), total pressure 1.3 bar, 200 °C, simulated concentrated sunlight (~1,100 mW/cm^2) irradiation.	0.924 mmol g^{-1} after 22 h	[15]
7	RuO_x(1 wt%)@MIL-125(Ti)-NH_2	Photocatalyst (15 mg), CO_2:H_2 (1:4), total pressure 1.3 bar, 200 °C, simulated concentrated sunlight (~1,100 mW/cm^2) irradiation.	~2.5 mmol g^{-1} after 22 h	[15]

selectivity is associated with the good chemisorption of reaction intermediates on RuO_x NPs, which favors their hydrogenation to CH_4.[15,27] In this work, to rationalize the high selectivity to CH_4 achieved with RuO_x-DMOF-350, *in situ* FT-IR measurements using CO as a probe molecule were carried (see results in Figure 6). The FT-IR spectrum of RuO_x-DMOF-350 after CO uptake until saturation is characterized by two bands centered at 2,178 and 2,153 cm^{-1} associated with CO chemisorption on oxidized RuO_x species (Figure 6a, blue line).[48] The absence of FT-IR band at about 2,050 cm^{-1} indicated that CO chemisorption on the metallic Ru(0) species present in RuO_x-DMOF-350, as previously characterized by XPS, should be negligible.[48] The system was then evacuated under vacuum. The resulting FT-IR spectrum of RuO_x-DMOF-350 was characterized by the absence of the previous band at 2,153 cm^{-1}, while the band at 2,178 cm^{-1} remained practically unmodified. These results show that oxidized RuO_x species in RuO_x-DMOF-350 are able to chemisorb CO, which can favor photocatalytic CO_2 hydrogenation to CH_4.[49]

Other studies have also reported that the reducibility of supported RuO_x NPs as active sites during CO_2 reduction can determine the resulting activity.[27,50] In this work, RuO_x-DMOF-350 and RuO_x-DMOF-650 were selected for this purpose, as they provided the highest and lowest photocatalytic activities. In particular, TPR-H_2 was used to evaluate RuO_x species reducibility in these solids.[51,52] TPR-H_2 profiles of RuO_x-DMOF-350 and RuO_x-DMOF-650 were respectively characterized by the presence of a main hydrogen consumption band at about 120 and 180 °C associated with the partial reduction of supported RuO_x species (Figure 6b).[51,52] The less intense broad bands extending from about 300 to 700 °C were attributable to the partial reduction of TiO_2-based support.[51] Interestingly, the easier reducibility of RuO_x in RuO_x-DMOF-350 than in the RuO_x-DMOF-650 sample agrees with the higher photocatalytic activity of the former. These observations are in line with previous studies that highlighted the role of reduced Ru species like Ru(0) as active sites during H_2 activation and the subsequent CO_2 reduction.[53]

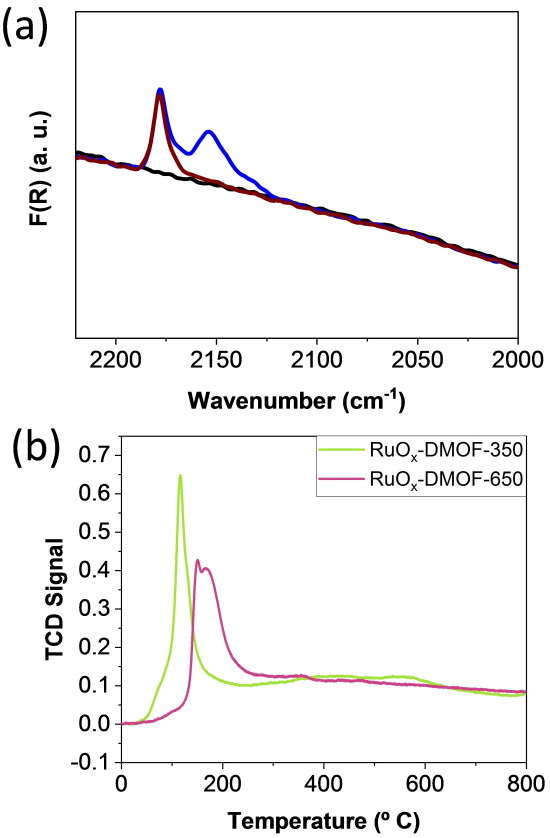

Figure 6. (a) FT-IR spectra upon CO adsorption over RuO_x-DMOF-350 sample and (b) TPR-H_2 spectra of RuO_x-DMOF-350 and RuO_x-DMOF-650 solids.

To further study the higher photocatalytic activity of the RuO_x-DMOF-350 sample, a comparative (photo)electrochemical study of RuO_x-DMOF solids was carried out to determine their relative photoinduced charge separation efficiencies. The EIS is frequently used to determine photocatalysts' relative charge transfer resistance and the results can be visualized by the so-called Nyquist plot.[54] In this work, the smallest Nyquist radii achieved from the RuO_x-DMOF-350 sample agreed with both the lowest charge transfer resistance and highest photocatalytic activity. The RuO_x-DMOF-450 and RuO_x-DMOF-550 solids have similar Nyquist radii and photocatalytic activities, while the RuO_x-DMOF-650 sample showed the longest Nyquist radii and the lowest activity (Figure 7a). To quantify the obtained EIS data, a simplified Randles equivalent circuit was employed to fit each Nyquist spectrum.[50] This electrical circuit consists of a solution resistance, a double layer capacitor and a charge transfer resistance (R_{ct}). The estimated R_{ct} for RuO_x-DMOF-350, RuO_x-DMOF-450, RuO_x-DMOF-550 and RuO_x-DMOF-650 were 2868, 4483, 4876 and 5402 Ω, respectively. Furthermore, an analogous EIS measurement under simulated sunlight irradiation was carried out using RuO_x-DMOF-350 that exhibited the highest photocatalytic activity. Interestingly, this experiment showed that the irradiation, that promotes photoinduced charge separation, reduces the charge transfer resistance of the sample. This result further supports the good performance observed for RuO_x-DMOF-350 photocatalyst under simulated sunlight irradiation. In agreement with the EIS conclusions, transient photocurrent measurements under simulated sunlight irradiations (Figure 7b) showed that RuO_x-DMOF-350 supported on a carbon substrate electrode had the highest current density of the series of samples under simulated sunlight irradiation. A similar experiment carried out in the presence of methanol as sacrificial electron donor resulted in an enhanced measured current intensity (Figure 7c). This result reinforces the finding that irradiation of RuO_x-DMOF-350 generates the charge carriers, holes and electrons, respectively, responsible for methanol oxidation and current generation. Furthermore, RuO_x-DMOF-350 resulted to be the sample that exhibits the highest photocurrent intensity in the presence of methanol compared to RuO_x-DMOF-450, RuO_x-DMOF-550 or RuO_x-DMOF-650, an observation that agrees with the highest photocatalytic activity of the former (Figure S29). The photoinduced charge separation efficiency of the RuO_x-DMOF samples was also studied by PL spectroscopy. Related studies have reported that the PL emission spectra of these type of solids can be associated to the recombination of the photoinduced charge carriers, the highest the emission intensity correlated with the highest

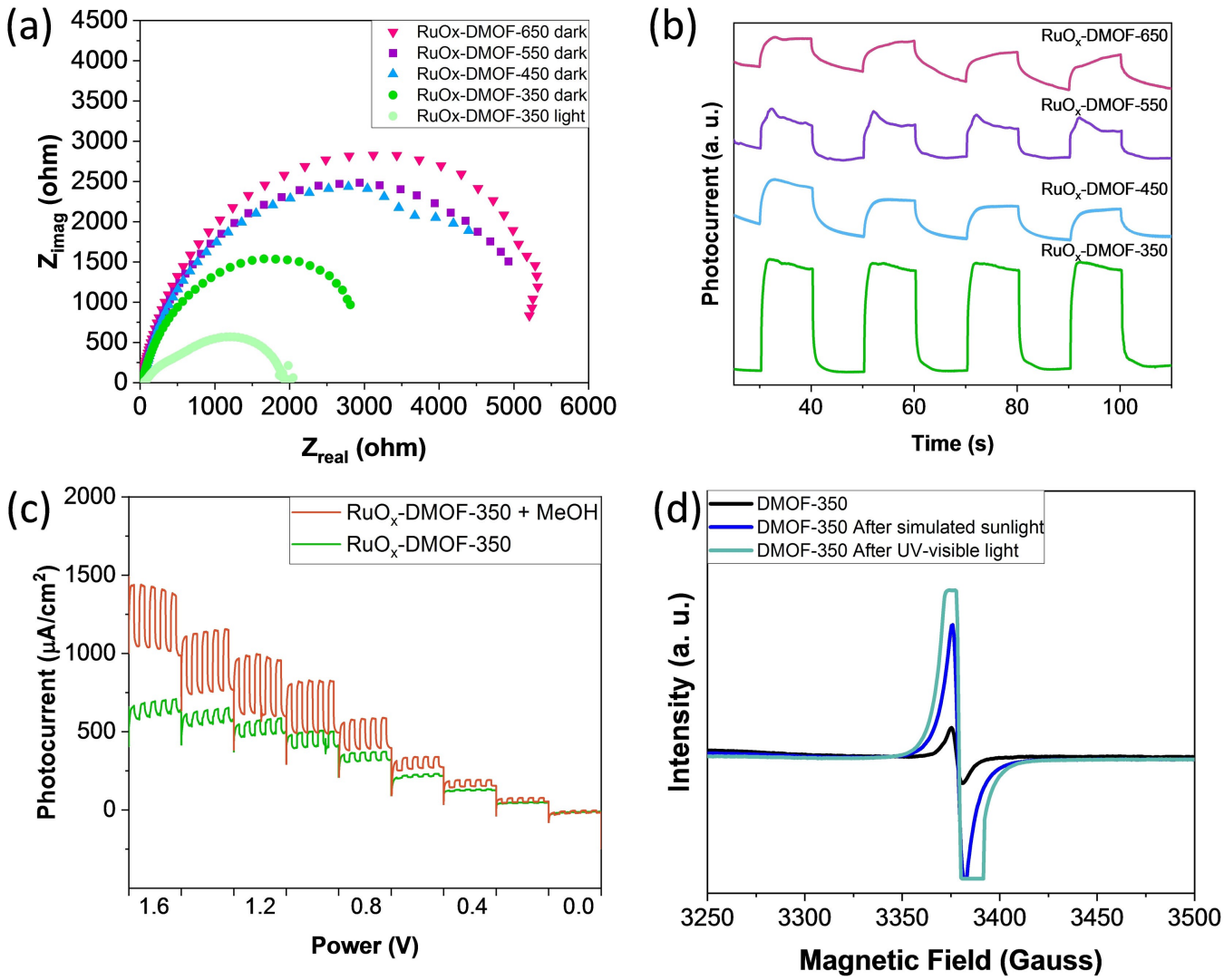

Figure 7. (a) EIS results for RuO_x-DMOF solids. (b) Current response of RuO_x-DMOFs supported on a carbon paper substrate electrode and immersed in acetonitrile (0.1 M, NBu_4PF_6) solution or (c) in a mixture of acetonitrile and methanol (0.3 mL) solution upon polarization from 1.6 to 0 V vs. Ag/AgCl during consecutive on/off cycles with simulated sunlight irradiation. (d) ESR spectra of RuO_x-DMOF-350 with or without light irradiation.

charge carrier recombination.[55] In our case, it is interesting to note that the order of photocatalytic activity is in accordance with the order of PL emission intensity (Figure S30), RuO_x-DMOF-350 exhibited the lowest PL emission, thus showing the highest photocatalytic activity. Overall, it can be concluded that the RuO_x-DMOF-350 sample has the lowest charge transfer resistance, the lowest charge carrier recombination and the highest photoinduced charge separation efficiency of the series of photocatalysts, and these factors favor its higher photocatalytic activity.

ESR spectroscopy was then used to study the active sites present on RuO_x-DMOF-350. The ESR spectrum of RuO_x-DMOF-350 shown in Figure 7d is characterized by two main regions. One of them can be assigned to the presence of Ti(III) species based on the determined g value of 1.979.[56] The other broad region can be associated to the presence of trapped holes (O^-) and/or surface adsorbed superoxide ($O_2^{\cdot-}$) species, based on the determined g value of 2.003.[56] The recorded ESR spectrum of RuO_x-DMOF-350 after simulated sunlight irradiation also shows the presence of these two regions. The small increase in intensity of the region of trapped holes and/or adsorbed superoxide compatible with the role of O^{2-} a hole trapping sites and/or formation of additional superoxide due to reaction of oxygen in air either with photogenerated electrons of by oxidizing Ti(III) species.[56,57] The small decrease in intensity of the region of Ti(III) species attributed to their reaction with molecular oxygen present in air and formation of superoxide species.[56,57] These ESR observations are compatible with EIS and transient photocurrent results, and it agrees with the occurrence of photoinduced charge separation in RuO_x-DMOF-350 upon simulated sunlight irradiation.

Figure 8 summarizes the proposed reaction mechanism that takes place during CO_2 methanation using RuO_x-DMOF-350 as a photocatalyst. As it has been commented, RuO_x-DMOF-350 is an active and selective thermocatalyst during CO_2 methanation at 200 °C (1.1 mmol g^{-1} CH_4 in 22 h). In addition, the activity of the

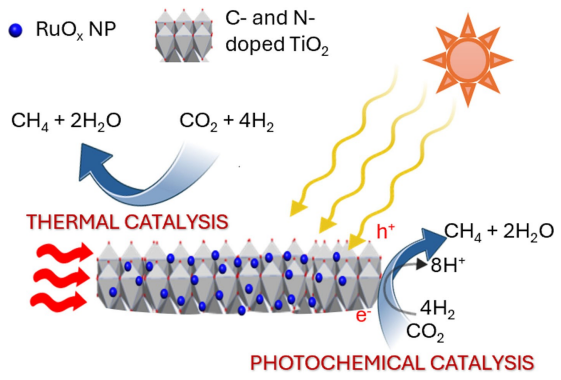

Figure 8. Proposed reaction mechanism for CO_2 methanation using RuO_x-DMOF-350 as a photocatalyst.

process can be enhanced by irradiation of RuO_x-DMOF-350 with the simulated sunlight due to the generation of electrons and holes responsible for CO_2 reduction and H_2 oxidation, respectively. Overall, the photocatalytic CO_2 hydrogenation to CH_4 using RuO_x-DMOF-350 can occur through a dual thermal and photochemical catalytic process.

3. Conclusions

This paper describes the development of an optimized RuO_x-DMOF-350 photocatalyst for gaseous and solar-assisted CO_2 methanation by H_2. The series of as-prepared materials were synthesized by calcination of a previously reported benchmark RuO_x@MIL-125(Ti)-NH_2 MOF-based photocatalyst at 350, 450, 550 and 650 °C for 4 h. The characterization data revealed that calcination of RuO_x@MIL-125(Ti)-NH_2 produces the formation of C- and N-doped-TiO_2 materials with anatase and/or rutile phases as the calcination temperature increases from 350 to 650 °C and is decorated with metallic and oxidized Ru species. All the materials are active photocatalysts for CO_2 methanation under relatively mild reaction conditions in terms of simulated sunlight irradiation intensity (45 mW/cm^2), temperature (< 200 °C) and total gas pressure (1.5 bar). RuO_x-DMOF-350 is the most active photocatalyst of the series (4.73 mmol g^{-1} at 22 h and AQY at 400, 500 and 750 nm of 0.76, 0.65 and 0.54%, respectively) and exhibited higher activity than some previously reported MOF-based photocatalysts for the same purpose. In addition, this photocatalyst was found to be stable and reusable for four consecutive cycles with an accumulated reaction time of 88 h. The achieved order of photocatalytic activities using RuO_x-DMOF-350 samples correlated with their photoinduced charge separation efficiency, as shown by transient photocurrent, EIS, ESR and PL and RuO_x reducibility as revealed by the TPR-H_2 technique. Overall, RuO_x-DMOF-350 can operate under a dual thermal and photochemical reaction pathways during gaseous and selective CO_2 hydrogenation to CH_4.

The authors consider that these findings will pave way for the development of MOF-derived photocatalysts with enhanced activities in solar-assisted processes.

Supporting Information Summary

Additional characterization details like powder XRD, TEM, SEM, SEM-mapping, TGA, BET, XPS, UV-Vis DRS, Tauc plots, Raman spectra, GC-MS and Photoluminescence spectra for RuO_x-DMOF solids are provided in the supporting information file.

Acknowledgements

C.M.R.N. thanks the support of PRE2019-089877 funded by MICIU/AEI/10.13039/501100011033. M.G.F. thanks the support of PRE2022-101327 funded by MICIU /AEI/10.13039/501100011033. A.D. is beneficiary of a grant María Zambrano in Universitat Politècnica de València within the framework of the grants for the retraining in the Spanish university system (Spanish Ministry of Universities, financed by the European Union, NextGeneration EU). The METHASOL project receives funding from the European Union Horizon 2020 research and innovation programme under Grant Agreement N°10102264. Funding for open access charge: CRUE-Universitat Politècnica de València. H.G.B. Thanks the support of grant number RYC2022-037287-I funded by MCIN/AEI/10.13039/501100011033. S.N. thanks the support of grant PID2021-123856OBI00 funded by MICIU/AEI/10.13039/501100011033 and by ERDF A way of making Europe.

Conflict of Interests

The authors declare no conflict of interest.

Data Availability Statement

The data that support the findings of this study are available on request from the corresponding author. The data are not publicly available due to privacy or ethical restrictions.

Keywords: Photocatalysis · Semiconductors · Metal-organic framework-derived · CO_2 methanation · Sunlight irradiation

[1] T. M. Gür, *Prog. Energy Combust. Sci.* **2022**, *89*, 100965.
[2] S. A. Ali, T. Ahmad, *Inorg. Chem.* **2024**, *63*, 304–315.
[3] S. A. Ali, I. Sadiq, T. Ahmad, *Langmuir.* **2024**, *40*, 10414–10432.
[4] S. A. Ali, T. Ahmad, *Langmuir.* **2024**, *21*, 10835–10846.
[5] A. Mehtab, T. Ahmad, *ACS Catal.* **2024**, *14*, 691–702.
[6] P. Yang, Y. Huang, Z.-W. Zhang, N. Li, Y. Fan, *Dalton Trans.* **2020**, *49*, 10052–11005.
[7] K. R. Thampi, J. Kiwi, M. Graetzel, *Nature* **1987**, *327*, 506–508.
[8] S. Kattel, P. Liu, J. G. Chen, *J. Am. Chem. Soc.* **2017**, *139*, 9739–9754.
[9] M. Younas, L. L. L. Kong, M. J. K. Bashir, H. Nadeem, A. Shehzad, S. Sethupathi *Energy Fuels.* **2016**, *30*, 8815–8831.
[10] A. Bolt, I. Dincer, M. Agelin-Chaab *J. Nat. Gas Sci. Eng.* **2020**, *84*. 103670.
[11] S. Rönsch, J. Schneider, S. Matthischke, M. Schlüter, M. Götz, J. Lefebvre, P. Prabhakaran, S. Bajohr, *Fuel.* **2016**, *166*, 276–296.
[12] M. A. A. Aziz, A. A. Jalil, S. Triwahyono, A. Ahmad, *Green Chem.* **2015**, *17*, 2647–2663.

[13] C. Tébar-Soler, V. Martin-Diaconescu, L. Simonelli, A. Missyul, V. Perez-Dieste, I. J. Villar-García, J.-B. Brubach, P. Roy, M. Lopez Haro, J. J. Calvino, P. Concepción, A. Corma, *Nat. Mater.* **2023**, *22*, 762–768.
[14] M. Cabrero-Antonino, S. Remiro-Buenamañana, M. Souto, A. A. García-Valdivia, D. Choquesillo-Lazarte, S. Navalón, A. Rodríguez-Diéguez, G. Mínguez-Espallargas, H. García, *Chem. Commun.* **2019**, *55*, 10932–10935.
[15] M. Cabrero-Antonino, B. Ferrer, H. G. Baldoví, S. Navalón, *Chem. Eng. J.* **2022**, *445*, 136426.
[16] S. Wang, M. Cabrero-Antonino, S. Navalón, C.-C. Cao, A. Tissot, I. Dovgaliuk, J. Marrot, C. Martineau-Corcos, L. Yu, H. Wang, W. Shepard, H. García, C. Serre, *Chem.* **2020**, *6*, 3409–3427.
[17] C. M. Rueda-Navarro, Z. Abou-Khalil, A. Melillo, B. Ferrer, R. Montero, A. Longarte, M. Daturi, I. Vayá, M. El-Roz, V. Martínez-Martínez, H. G. Baldoví, S. Navalón, *ACS Catal.* **2024**, *14*, 6470–6487.
[18] M. Cabrero-Antonino, A. Melillo, E. Montero-Lanzuela, M. Álvaro, B. Ferrer, I. Vayá, H. G. Baldoví, S. Navalón, *Chem. Eng. J.* **2023**, *468*, 143553.
[19] D. Huang, G. Wang, M. Cheng, G. Zhang, S. Chen, Y. Liu, Z. Li, W. Xue, L. Lei, R. Xiao, *Chem. Eng. J.* **2021**, *421*, 127817.
[20] X. Li, D. Wu, T. Hua, X. Lan, S. Han, J. Cheng, K.-S. Du, Y. Hu, Y. Chen, *Sci. Total Environ.* **2022**, *804*, 150096.
[21] C. Wang, J. Kim, V. Malgras, J. Na, J. Lin, J. You, M. Zhang, J. Li, Y. Yamauchi, *Small.* **2019**, *15*, 1900744.
[22] P. Behera, S. Subudhi, S. P. Tripathy, K. Parida, *Coord. Chem. Rev.* **2022**, *456*, 214392.
[23] X. He, M. Wu, Z. Ao, B. Lai, Y. Zhou, T. An, S. Wang, *J. Hazard. Mater.* **2021**, *403*, 124048.
[24] C. Zhao, Z. Wang, X. Chen, H. Chu, H. Fu, C. C. Wang, *Chin. J. Catal.* **2020**, *41*, 1186–1197.
[25] B. Yan, L. Zhang, Z. Tang, M. Al-Mamunc, H. Zhao, X. Su, *Appl. Catal. B. Environ.* **2017**, *218*, 743–750.
[26] I. S. Khan, D. Mateo, G. Shterk, T. Shoinkhorova, D. Poloneeva, L. Garzón-Tovar, J. Gascon, *Angew. Chem. Int. Ed.* **2021**, *60*, 26476–26482.
[27] H. Wang, Q. Li, J. Chen, J. Chen, H. Jia, *Adv. Sci.* **2023**, *10*, 2304406.
[28] F. Almazán, M. Lafuente, A. Echarte, M. Imizcoz, I. Pellejero, L. M. Gandía, *Chemistry.* **2023**, *52*, 720–729.
[29] I. S. Khan, L. Garzon-Tovar, D. Mateo, J. Gascon, *Eur. J. Inorg. Chem.* **2022**, *28*, e202200316.
[30] D. Mateo, J. L. Cerrillo, S, Durini, J. Gascon, *Chem. Soc. Rev.* **2021**, *50*, 2173–2210.
[31] C. M. Rueda-Navarro, B. Ferrer, H. G. Baldoví, S. Navalon, *Nanomaterials.* **2022**, *12*, 3808.
[32] H. A. Mahmoud, K. Narasimharao, T. T. Ali, K. M. S. Khalil, *Nanoscale Res. Lett.* **2018**, *13*, 48.
[33] X. Song, J. He, Y. Wang, J. Wang, S. Zhang, *J. Colloid Interface Sci.* **2023**, *645*, 918–932.
[34] W. Wang, W. Qiang, C. Chen, D. Sun, *Polymers* **2024**, *16*, 186.
[35] D. A. H. Hanaor, C. C. Sorrel, *J. Mater. Sci.* **2010**, *46*, 855–874.
[36] D. Bersani, G. Antonioli, P. P. Lottici, T. Lopez, *J. Non-Cryst. Solids.* **1998**, *232–234*, 175–181.
[37] J. Cored, A. García Ortiz, S. Iborra, M. J. Climent, L. Liu, C.-H. Chuang, T.-S. Chan, C. Escudero, P. Concepción, A. Corma, *J. Am. Chem. Soc.* **2019**, *141*, 19304–19311.
[38] A. Sadezky, H. Muckenhuber, H. Grothe, R. Niessner, U. Pöschl, *Carbon.* **2005**, *43*, 1731–1742.
[39] S. Chen, A. M. Ali, D. Li, J. Bansmann, S. Cisneros, J. Biskupek, W. Huang, R. J. Behm, *Angew. Chem. Int. Ed.* **2019**, *58*, 10732–10736.
[40] D.-E. Gu, Y. Lu, B.-C. Yang, Y.-D. Hu, *Chem. Commun.* **2008**, 2453–2455.
[41] P. M. Korusenko, S. N. Nesov, S. N. Povoroznyuk, P. V. Orlov, D. N. Korotaev, K. N. Poleschenko, E. E. Tarasov, *Data in brief.* **2019**, *27*, 104737.
[42] Y. Jiang, Y. Qin, T. Yua, S. Lin, *Chin. Chem. Lett.* **2021**, *32*, 1823–1826.
[43] B. Chen, J. Sha, W. Li, F. He, E. Liu, C. Shi, C. He, J. Li, N. Zhao, *ACS Appl. Mater. Interfaces.* **2016**, *8*, 2495–2504.
[44] S. Dai, Y. Wu, T. Sakai, Z. Du, H. Sakai, M. Abe, *Nanoscale Res. Lett.* **2010**, *5*, 1829–1835.
[45] Z. Xiao, X. Jiang, B. Li, X. Liu, X. Huang, Y. Zhang, Q. Ren, J. Luo, Z. Qin, J. Hu, *Nanoscale* **2015**, *7*, 11962–11970.
[46] J. Ren, S. Ouyang, H. Xu, X. Meng, T. Wang, D. Wang, J. Ye *Adv. Energy Mater.* **2016**, 1601657.
[47] L. Chen, I. A. W. Filot, E. J. M. Hensen, *ACS Catal.* **2023**, *13*, 15230–15247.
[48] J. Aßmann, E. Löffler, A. Birkner, M. Muhler, *Catal. Today.* **2003**, *85*, 235–249.
[49] P. Panagiotopoulou, *Appl. Catal. B. Environ.* **2018**, *236*, 162–170.
[50] M. Zielinski, E. Janiszewska, A. Drewniak, M. Pietrowski, *Molecules.* **2023**, *28*, 6376.
[51] J. Shi, F. Hui, J. Yuan, Q. Yu, S. Mei, Q. Zhang, J. Li, W. Wang, J. Yang, J. Lu, *Catalysts.* **2019**, *9*, 108.
[52] T. Sakpal, L. Lefferts, *J. Catal.* **2018**, *367*, 171–180.
[53] J. Zhai, Z. Xia, B. Zhou, H. Wu, T. Xue, X. Chen, J. Jiao, S. Jia, M. He, B. Han, *Nat. Commun.* **2024**, *15*, 1109.
[54] J. Ângelo, P. Magalhães, L. Andrade, A. Mendes, *Appl. Surf. Scie.* **2016**, *387*, 183–189.
[55] A. Dhakshinamoorthy, Z. Li, S. Yang, H. Garcia, *Chem. Soc. Rev.* **2024**, *53*, 3002–3035.
[56] S. Maurelli, M. Vishnuvarthan, G. Berlier, M. Chiesa, *Phys. Chem. Chem. Phys.* **2012**, *14*, 987–995.
[57] S. K. Misra, S. I. Andronenko, D. Tipikin, J. H. Freed, V. Somani, O. Prakash, *J. Magn. Magn. Mater.* **2016**, *401*, 495–505.

Manuscript received: June 12, 2024
Revised manuscript received: August 6, 2024
Accepted manuscript online: August 10, 2024
Version of record online: October 9, 2024